

Numerical study of the effects of chemical dispersant on oil transport from an idealized underwater blowout

Bicheng Chen

*Department of Meteorology and Atmospheric Science, Pennsylvania State University,
University Park, Pennsylvania 16802, USA*

Di Yang

Department of Mechanical Engineering, University of Houston, Houston, Texas 77204, USA

Charles Meneveau

Department of Mechanical Engineering, Johns Hopkins University, Baltimore, Maryland 21218, USA

Marcelo Chamecki*

*Department of Atmospheric and Oceanic Sciences, University of California,
Los Angeles, Los Angeles, California 90095, USA*



(Received 10 January 2018; published 6 August 2018; corrected 27 August 2018)

As part of the response efforts that followed the Deepwater Horizon oil spill event, chemical dispersants were applied at the ocean surface and at the wellhead to increase biodegradation rates and reduce the environmental impact of the spill. Among other factors, the effectiveness of the application hinges on how it modifies complex fluid mechanical transport processes. The breakup of surface slicks and the vertical dilution of oil in the water column depends on the transport of oil droplets by turbulence in the ocean mixed layer. The trapping of oil deep in the water column results from the complex dynamics of multiphase plumes rising in the stratified ocean. We use a framework based on multiscale coupled computational domains to simulate deep-water blowouts that accurately represents these complex processes, tracking the oil from the wellhead to its transport in the ocean mixed layer. Simulation results show that dispersant application at the wellhead can be effective in trapping the oil in deep-water intrusions. For the conditions simulated here, surface application of the dispersant has important effects on the oil transport: after about 40 h, the mean advection velocity of the oil plume is reduced by a factor of four and the horizontal diffusivity is increased by a factor of 10.

DOI: [10.1103/PhysRevFluids.3.083801](https://doi.org/10.1103/PhysRevFluids.3.083801)

I. INTRODUCTION

The Deepwater Horizon (DWH) oil spill following the accident on April 20, 2010, was the largest oil spill in history, having triggered a massive response effort that has cost tens of billions of dollars [1]. As part of the response, about 1.4 million gallons of dispersant were applied at the ocean surface, and 0.77 million gallons were applied in deep water near the wellhead [2]. Although most of the controversy associated with the decision to use chemical dispersants is centered around potential unintended consequences, such as exposure of benthic organisms to oil [3] and the toxicity of dispersants themselves [4–6], the effectiveness of its application is determined by how

*chamecki@ucla.edu

the reduction in droplet size alters complex fluid mechanical transport processes. Thus, anticipating the consequences of dispersant application on the fate of the oil requires a clear understanding of the different stages of the oil plume as it rises through the water column and forms surface slicks.

At the initial stage of a deep-water spill, termed the near field, the multiphase plume of oil droplets and gas bubbles rises mostly driven by the buoyancy of the gas bubbles. As the plume rises in a stably stratified environment it entrains ambient fluid, transporting it upwards in the water column and reducing the overall plume buoyancy [7,8]. After the plume buoyancy becomes negative, at the peel height, a large fraction of entrained fluid peels off carrying small oil droplets with it. The peeled fluid falls to the depth of neutral buoyancy, the trap height, forming an intrusion layer [9,10]. The intrusion layer traps the peeled fluid and the weakly buoyant oil droplets, increasing the opportunity for biodegradation in deep waters, but also increasing risks to deep-water ecosystems. The main purpose of dispersant application at the wellhead is to reduce the size of oil droplets, which both increases the surface-to-volume ratio and decreases the buoyancy of oil droplets, so that most of the oil is trapped deep in the water column until it is biodegraded. In the absence of wellhead application, the larger oil droplets have large enough buoyancy to continue rising. Once the oil plume reaches the ocean mixed layer (OML), the oil forms large surface slicks. Its transport on the surface, termed the far field, is then governed by a number of physical processes including Ekman transport, mesoscale and submesoscale eddies, surface waves, Langmuir circulations, and small-scale three-dimensional (3D) turbulence. The purpose of surface applications is to break up the surface slick into small oil droplets that can be transported back into the water column, accelerating biodegradation and reducing the risk of oil reaching sensitive shorelines and habitats [11]. This process depends critically on how turbulence and surface waves interact with buoyant droplets of different sizes.

Most of the numerical studies of transport and fate of oil plumes from the Deepwater Horizon event have relied on regional ocean modeling [12–17]. While this approach has great capability in representing mean currents and mesoscale features (which dominate the large-scale structure of plumes in the far field), it relies on simple parametrizations of the fluid mechanical processes outlined above. For example, Paris *et al.* [15] and Testa *et al.* [17] studied the effects of deep-water application of dispersants on the amount of oil reaching the surface. While neither of these studies explicitly resolved the dynamics of the multiphase plume, the conclusion seems to be that if the oil droplet size in the rising plume is fairly large (say, larger than $500\ \mu\text{m}$), the application of dispersants can effectively reduce the amount of surfacing oil [17]. Up to now, numerical simulations resolving the near-field dynamics have been restricted to more idealized conditions [8,18–20]. Similarly, numerical simulations of the far-field oil transport rely on parametrization of the vertical and horizontal eddy diffusivities, which do not include important effects such as those caused by the presence of Langmuir cells. Simulations that resolve turbulence in the OML have been confined mostly to small domains and based on various idealizations [21–23]. Nevertheless, these studies have uncovered the critical role of oil droplet size on the transport of oil in the OML, suggesting that even the mean transport direction depends on the size of oil droplets [22].

In this study we deployed a numerical tool based on the large-eddy simulation (LES) technique to investigate oil transport from deep-water blowouts, capable of accurately representing the dynamical processes in the near and far fields simultaneously. The approach combined simulations of near-field LES with far-field ENDLESS (extended nonperiodic domain LES for scalar transport), a recently proposed multiscale approach that enables simulating very large scalar plumes in the far field while still capturing small-scale turbulence in the advecting velocity field [24]. Simulations were used to investigate the fundamental fluid mechanical processes responsible for the effects of droplet size reduction promoted by chemical dispersants on the trapping of oil droplets in the intrusion layers and the surface transport in the OML. More specifically, the effects of surface dispersant on the transport velocity and horizontal diffusivity of oil plumes in the OML were quantified, and the dependence of horizontal diffusivity on plume size was compared to observational data for near-surface tracers [25–28].

II. NUMERICAL SIMULATION

The different scales and physical processes governing the dynamics of the oil plume in the near and far fields require different numerical simulation strategies. The numerical tool developed here consists of two separate domains for the near and far fields. The near-field domain was used to simulate the multiphase plume of gas bubbles and oil droplets originating from the wellhead and rising through the 1.5 km stratified water column, capturing the formation of deep-water intrusions and the separation of oil and gas plumes due to weak crossflow. Even though the near-field simulation domain extended up to the surface of the ocean, the vertical resolution was not enough to properly resolve processes in the OML. Therefore, instantaneous oil concentration at a depth $z = -150$ m obtained from the near-field domain was used as a plume inflow condition for the far-field domain (see Fig. 1). The far-field domain was used to simulate the oil transport in the OML in response to submesoscale eddies, surface waves, Langmuir cells, and 3D small-scale turbulence. Both simulations were based on the same basic LES implementation, which is described in detail by Yang *et al.* [22] and only briefly reviewed here.

The dynamical core was based on the filtered Craik-Lebovich equations [29–31], so that surface gravity waves were not resolved, but their phase-averaged effects were represented by terms associated with the Stokes drift velocity \mathbf{u}_s . The equation employed in this study is given by

$$\frac{\partial \tilde{\mathbf{u}}}{\partial t} + \tilde{\mathbf{u}} \cdot \nabla \tilde{\mathbf{u}} = -\frac{1}{\rho_0} \nabla \tilde{p} - \nabla \cdot \boldsymbol{\tau} + \left(1 - \frac{\tilde{\rho}}{\rho_0}\right) g \mathbf{e}_3 - 2\boldsymbol{\Omega} \times \tilde{\mathbf{u}} + \tilde{\mathbf{f}}_{bu} + \tilde{\mathbf{f}}_s + \tilde{\mathbf{f}}_{bg} \quad (1)$$

together with the incompressibility condition $\nabla \cdot \tilde{\mathbf{u}} = 0$. Here a tilde denotes a variable resolved on the LES grid, \mathbf{u} is the Eulerian velocity, p is a modified pressure, and $\boldsymbol{\tau} = (\tilde{\mathbf{u}}\tilde{\mathbf{u}} - \tilde{\mathbf{u}}\tilde{\mathbf{u}})$ is the subgrid-scale (SGS) stress tensor. In addition, g is the gravitational acceleration, \mathbf{e}_3 is the unit vector in the vertical direction, ρ_0 is the reference density of sea water, ρ is the density of sea water, and $\boldsymbol{\Omega}$ is the angular velocity of Earth. The remaining forces on the right-hand side of Eq. (1) are the additional buoyancy force due to the mass concentrations of monodisperse gas bubbles (\tilde{C}_b) and oil droplets (\tilde{C}_o) given by [8]

$$\tilde{\mathbf{f}}_{bu} = \left(1 - \frac{\tilde{C}_o}{\rho_0} - \frac{\tilde{C}_b}{\rho_0}\right) g \mathbf{e}_3, \quad (2)$$

and the forces associated with the Stokes drift [32]

$$\tilde{\mathbf{f}}_s = -2\boldsymbol{\Omega} \times \mathbf{u}_s + \mathbf{u}_s \times \tilde{\boldsymbol{\omega}}. \quad (3)$$

Here $\boldsymbol{\omega}$ is the vorticity field. Finally, the additional force

$$\tilde{\mathbf{f}}_{bg} = +2\boldsymbol{\Omega} \times (U_{bg} \mathbf{e}_1) \quad (4)$$

was used to superimpose a steady and uniform background (geostrophic) flow velocity U_{bg} in the x direction (indicated by the unit vector \mathbf{e}_1). This velocity was used to model a flow perpendicular to the rising plume, which caused a horizontal separation between the plumes of gas bubbles and oil droplets after the peeling process took place. Note that the use of this forcing ensures that the background flow velocity is already included in the filtered velocity field $\tilde{\mathbf{u}}$.

Gas bubbles and oil droplets were described as mass concentration fields $C_a(\mathbf{x}, t)$ in continuous Eulerian form (hereafter $a = b$ is used for gas bubbles and $a = o$ for oil droplets). These concentration fields were evolved by filtered advection-diffusion equations of the form

$$\frac{\partial \tilde{C}_a}{\partial t} + \nabla \cdot (\tilde{\mathbf{v}}_a \tilde{C}_a) = -\nabla \cdot \boldsymbol{\pi}_a + Q_a, \quad (5)$$

where $\tilde{\mathbf{v}}_a$ is the dispersed phase velocity associated with the concentration field C_a (to be specified later), $\boldsymbol{\pi}_a = (\tilde{\mathbf{u}}\tilde{C}_a - \tilde{\mathbf{u}}\tilde{C}_a)$ is the SGS concentration flux, and Q_a is a source term. The advection

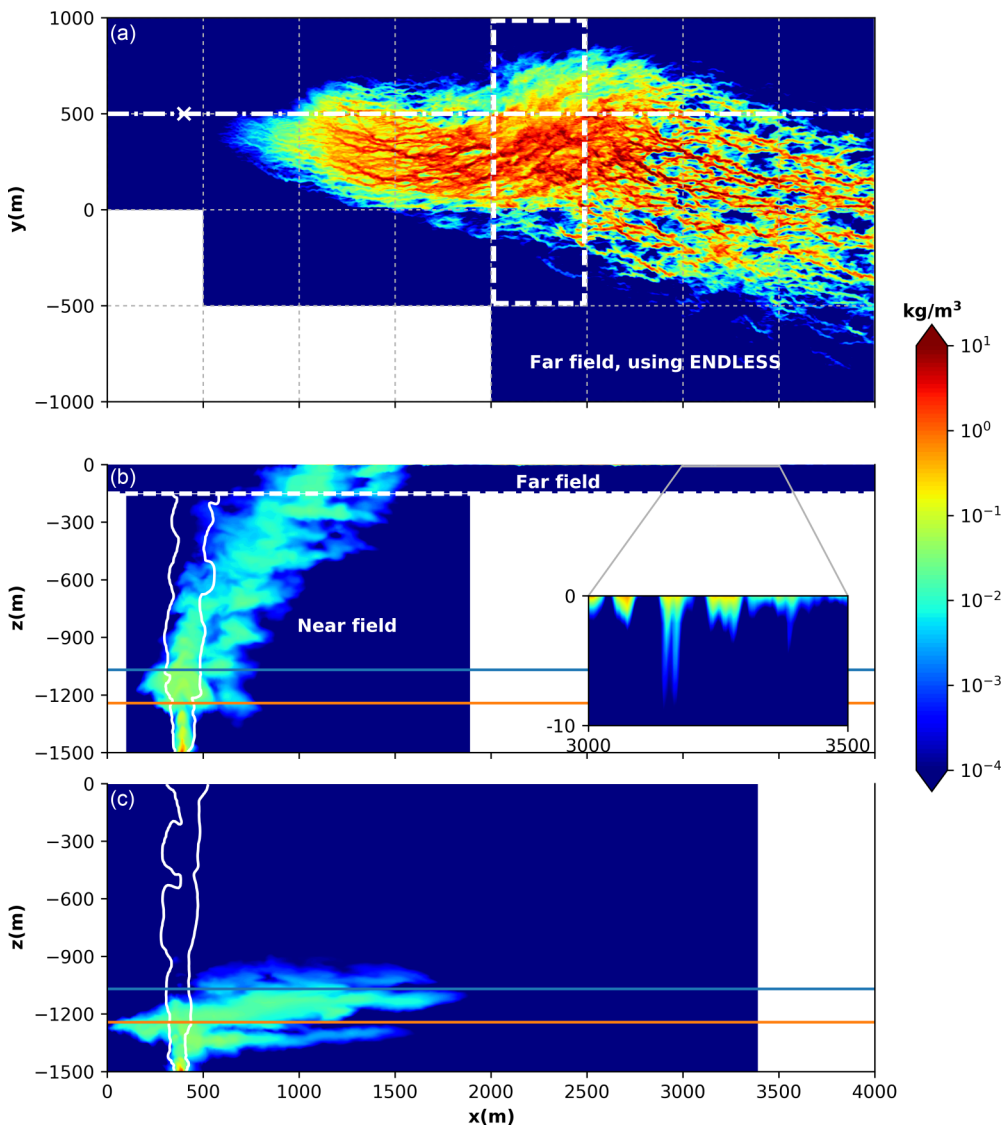


FIG. 1. (a) Surface oil concentration from the far-field domain just before surface dispersant application with target area indicated by white dashed line. Dot-dashed line indicates position of cuts for panels (b) and (c), and the source location is indicated by a cross. The white dashed line in panel (b) indicates the interface between near-field and far-field domains. Thin gray dashed lines indicate the “velocity-field LES domain”. (b) and (c) Cross section through the source showing the rising oil plume and the core of the bubble plume (white contours) for simulations without and with dispersant application at the wellhead, respectively. Blue and orange lines indicate positions of mean peel and trap heights, respectively.

velocity of the dispersed phases (for both gas bubbles and oil droplets) was given by

$$\tilde{\mathbf{v}}_a = \left[\tilde{\mathbf{u}} + w_{r,a} \mathbf{e}_3 + \frac{w_{r,a}}{g} \frac{D\tilde{\mathbf{u}}}{Dt} \right] + \mathbf{u}_s + \mathbf{u}_{LS}, \quad (6)$$

where the terms in the squared brackets correspond to the Eulerian equilibrium approach [33], where $w_{r,a}$ is a constant bubble or droplet rise velocity in still fluid and the last term is an approximation for

the inertial correction valid for small Stokes number [33] (it is based on an asymptotic expansion in the Stokes number retaining only the first-order term). The last two terms are the Stokes drift velocity \mathbf{u}_s and a large-scale nondivergent flow component $\mathbf{u}_{L,S}$ not resolved in the LES and used only in the ENDLESS implementation for the far field (see details below).

For simplicity, a deep-water monochromatic wave field was adopted, with corresponding Stokes drift velocity given by $\mathbf{u}_s(z \leq 0) = \mathbf{e}_1 U_s e^{2kz}$, where $U_s = |\mathbf{u}_s(z=0)| = (2\pi a/\lambda)^2 \sqrt{g\lambda/2\pi}$ [22] is the magnitude of the surface Stokes drift velocity, a is the wave amplitude, λ is the wavelength, and $k = 2\pi/\lambda$ is the wave number.

Sea-water density was expressed in terms of potential temperature θ using the linear relation $\rho = \rho_0[1 - \alpha_\theta(\theta - \theta_0)]$, where α_θ is the thermal expansion rate and θ_0 is the reference potential temperature corresponding to the reference density ρ_0 . An additional advection-diffusion equation was solved for potential temperature with velocity $\tilde{\mathbf{v}}_\theta = \tilde{\mathbf{u}} + \mathbf{u}_s + U_{bg}\mathbf{e}_1$ and source $Q_\theta = 0$. SGS fluxes were parameterized using the Lilly-Smagorinsky model [34,35] with the Lagrangian scale-dependent dynamic model [36] and constant SGS Prandtl and Schmidt numbers $\text{Pr}_\tau = 0.4$ and $\text{Sc}_\tau = 0.8$ [22]. The specific details of each module and their coupling are described below. This implementation has been successfully used by Yang *et al.* [8] to reproduce laboratory experiments of buoyancy-driven multiphase plumes in a stratified environment [37], and it has been used in several studies of far-field oil plumes in the OML [21–24].

A. Near-field domain

The simulation setup for an idealized DWH scenario was mostly based on conditions used by Socolofsky *et al.* [38]. The vertical domain size was $L_z = 1500$ m, and gas bubbles and oil droplets were released from a localized source at the bottom of the domain, representing the release from the wellhead. The horizontal domain size was chosen to be $L_x \times L_y = 1800$ m \times 900 m. The discretization was performed on a uniform grid using $N_x \times N_y \times N_z = 192 \times 96 \times 256$ grid points. A larger domain with $L_x = 3600$ m and $N_x = 384$ points was used for the deep-water dispersant case. Plume rise was completely driven by buoyancy, as no momentum flux source was included at the wellhead. The environment was represented by a background flow with velocity $U_{bg} = 1.5$ cm/s, which falls in the range of a typical crossflow condition at the DWH region (up to 7.8 cm/s [38]). The water column was stratified below $z = -50$ m by specifying a quadratic density profile matching conditions near the DWH blowout [38]. This was accomplished by shifting down by 50 m the quadratic density profile from Socolofsky *et al.* [38], reducing the depth of the near-mixed region at the bottom and adding a well-mixed OML at the top of the profile. An additional simulation with no shift in the density profile was also performed to confirm that this shift caused only small differences in the predicted trap and peel heights.

The properties of the oil and gas plumes were specified as reported by Socolofsky *et al.* [38]. The volumetric release rate of gas and oil were set to 0.065 m³/s and 0.085 m³/s, respectively. Gas bubbles with an effective diameter of $d_b = 2.06$ mm and rise velocity fluid of $w_{r,b} = 21$ cm/s were used. Oil droplets with a diameter of $d_o = 710$ μm and rise velocity of $w_{r,o} = 2.15$ cm/s (based on empirical correlations [39,40]) were adopted. There has been a long debate about the droplet size distribution in the DWH [15,41–43], and no consensus has yet emerged [44]. Nevertheless, the droplet diameter adopted here yields estimates of surfacing time consistent with observations for the DWH spill as shown below.

If the buoyancy frequency of $N = 6.63 \times 10^{-4}$ s⁻¹ at the wellhead is used to characterize the flow, the conditions adopted here correspond to a nondimensional slip velocity $U_N = w_{r,b}/(B_s N)^{1/4} \approx 1.42$ (B_s being the kinematic buoyancy flux of oil and gas combined) suggesting the development of a clear intrusion layer [45]. The wellhead buoyancy flux also yields a Rossby number $\text{Ro} = N/f \approx 10$ (f being the Coriolis frequency, calculated here based on a latitude of 28.7°N), indicating that effects of rotation on near-field plume structure could be important [20,46]. Our simulation includes the complete Coriolis acceleration term and should capture any rotation effects. We note, however,

that N increases monotonically above the wellhead, and it is not clear how strong rotation effects may be.

B. Far-field domain

The far-field domain employed the multiscale ENDLESS approach [24], in which the velocity field is computed on a smaller horizontal domain termed the “velocity-field LES domain” and the oil plume is evolved on a much larger horizontal domain termed the “extended domain” (this is accomplished by leveraging the periodic boundary conditions used in the flow solver to replicate the velocity, potential temperature, and pressure fields). The ENDLESS technique is applicable only to passive scalars, so the buoyancy force exerted by oil droplets on the flow was neglected ($\tilde{\mathbf{f}}_{bu} = 0$) in the far-field domain (this is a reasonable assumption given the small buoyancy forcing that resulted from the oil concentrations simulated here). The bubble phase was not included in the far-field domain simulation, because the gas bubbles arrived in the OML at a different horizontal location from the oil droplets [see Fig. 1(b)] and would have had no effect on the oil plume.

For the present application, the “velocity-field LES domain” was set to $500 \text{ m} \times 500 \text{ m}$ in the horizontal directions and 150 m in the vertical direction with $100 \times 100 \times 150$ grid points. The initial depth of the OML was 50 m , and the simulation was driven by a constant wind stress $\tau_s = 0.037 \text{ N/m}^2$ imposed on the ocean surface in the x direction (corresponding to a friction velocity of $u_* = 6.1 \times 10^{-3} \text{ m/s}$ in the water and a wind speed of approximately 5 m/s at 10 m height). A Stokes drift profile with surface velocity $U_s = 0.0677 \text{ m/s}$ was adopted, corresponding to a monochromatic wave train with wavelength $\lambda = 60 \text{ m}$ and amplitude $a = 0.8 \text{ m}$. The corresponding turbulent Langmuir number [32] $La_t = \sqrt{u_*}/U_s$ was 0.3 , a typical value for fully developed wind-driven OML dominated by Langmuir turbulence [47,48]. The resulting drift-to-buoyancy parameter [21] $D_b = (U_s/w_{r,o}) = 3.15$ was in the “fingered” surface oil slicks regime ($D_b \lesssim 10$), indicating that most of the oil should remain on the surface (as in a real oil slick) and form high oil concentration regions on the surface convergence zones located at the top of the downwelling branches of the Langmuir cells.

ENDLESS also includes a framework to represent oil advection by large-scale nondivergent flow \mathbf{u}_{LS} . As done in Chen *et al.* [24], an idealized two-dimensional (2D) cellular flow was adopted here as a simple surrogate to illustrate the effects of advection by submesoscale and mesoscale eddies. This idealized 2D cellular flow was composed of two modes, and it was set up following Eqs. (8) in Chen *et al.* [24] with velocity scale of 2.5 cm s^{-1} and eddy diameters of 1 and 2.8 km . These parameters yielded Rossby numbers of 0.35 and 0.12 , respectively, which are in the range between submesoscale and mesoscale eddies.

C. Idealized dispersant simulations

Two separate simulations were performed to investigate the effects of dispersants applied at the surface and the wellhead. For the surface application, the simulation was first evolved for a total time of 26.7 h after release initiated at the wellhead [see Figs. 1(a) and 1(b)]. A target area for the dispersant application was arbitrarily chosen [a rectangle of 0.5 km by 1.5 km illustrated in Fig. 1(a)]. It was assumed that the dispersant was applied at once to the entire area and that all the oil droplets within that area broke up very quickly into smaller droplets of size $d_{o,dis} = 100 \mu\text{m}$ conserving the total oil mass (this choice of size is reasonable given that a 10-fold reduction in surface tension corresponds approximately to a 5-fold reduction in droplet size [49]). This smaller droplet size corresponds to a rise velocity of $8.64 \times 10^{-2} \text{ cm/s}$ and a drift-to-buoyancy parameter $D_b = 78.7$, being in the diluted plume regime ($D_b \gtrsim 25$) [21]. The oil outside the target area was not impacted in any way by the application of dispersant. From this point on, the simulation was split into three new simultaneous simulations based on the same velocity field: (1) a simulation for the oil plume outside the target area with original droplet size $d_o = 710 \mu\text{m}$, (2) a simulation only for the the oil patch within the target area with original droplet size, and (3) a simulation for the same oil patch with the reduced droplet

size $d_{o,\text{dis}} = 100 \mu\text{m}$. With these three simulations, which were carried out for additional 43 h, it was possible to reconstruct the entire plume with and without the application of surface dispersants.

For the simulation of the wellhead application, it was assumed that all the oil droplets were broken up into the same smaller diameter at the wellhead. Due to the much smaller rise velocity of oil droplets in this case, most of the oil was trapped in the deep-water region and only the near-field domain was used. A passive tracer was also included in the simulation to help in the estimation of the peel and trap heights, following the procedure used by Yang *et al.* [8].

D. Analysis of surface oil patches

For a quantitative analysis of the effects of surface dispersant on oil transport, Lagrangian metrics were used to track the evolution of the oil patches inside the target area. The center of mass of the oil patch $\mathbf{x}_{cm} = (x_{cm}, y_{cm}, z_{cm})$ is given by

$$\mathbf{x}_{cm}(t) = \frac{1}{M_{\text{tot}}} \iiint_V \mathbf{x} \tilde{C}_o(\mathbf{x}; t) dV, \quad (7)$$

where M_{tot} is the total mass of oil in the volume considered and $\mathbf{x} = (x, y, z)$ is the position vector. In addition, the velocity of the center of mass is given by $\mathbf{u}_{cm} = d\mathbf{x}_{cm}/dt$. The instantaneous plume or patch size can be defined using the second moment of the concentration

$$\sigma_i^2(t) = \frac{1}{M_{\text{tot}}} \iiint_V [x_i - x_{cm,i}(t)]^2 \tilde{C}_o(\mathbf{x}; t) dV. \quad (8)$$

Here the subscript i denotes the component of three directions ($i = 1, 2, 3$ corresponding to x, y, z directions, respectively), and no summation over i is implied in Eq. (8). The horizontal diffusivity can be determined from $K_i(t) = (1/2)d\sigma_i^2/dt$. For consistency with observational experiments of dye diffusion [26–28], in practice we approximate the rate of change of plume size always with respect to the initial size and define the apparent diffusivity

$$K_{a,i}(t - t_0) = \frac{\sigma_i^2(t) - \sigma_i^2(t_0)}{4(t - t_0)}, \quad (9)$$

where $t = t_0$ is the time of application of dispersant. Finally, the horizontal size of the patch is given by $\sigma_r = (\sigma_1^2 + \sigma_2^2)^{1/2}$, and the total apparent diffusivity with respect to the horizontal size σ_r is defined as

$$K_r = (1/2)(K_{a,1} + K_{a,2}). \quad (10)$$

Note that the true diffusivity $K_i(t)$ and the apparent diffusivity $K_{a,i}(t)$ have different values but follow the same power-law behavior. In dye experiments one typically has a point source so that $\sigma_r^2(t_0) \approx 0$, which is not the case here.

Following Richardson's 4/3 law [50] relating the eddy diffusivity to the scale of the diffusing plume ℓ (hereafter referred to as plume scale and taken to be $\ell = 3\sigma_r$), it has become common practice to display ocean horizontal apparent diffusivity as a function of ℓ and empirically fit a power law of the form $K_h(\ell) = \alpha \ell^\beta$ [25–28]. Note that this power law corresponds to a plume growth $\sigma_r^2(t) \propto t^{2/(2-\beta)}$, which recovers Fickian diffusion $\sigma_r^2(t) \propto t$ for a constant diffusivity ($\beta = 0$) and the well-known $\sigma_r^2(t) \propto t^3$ for Richardson diffusion ($\beta = 4/3$). Lawrence *et al.* [28] obtained $K_h(\ell) = 3.2 \times 10^{-4} \ell^{1.1}$ (with K_h in m^2/s and ℓ in m) by fitting several data sets of dye dispersion in shallow water. For comparison with these data, horizontal diffusivities from the present simulations were averaged conditioned on the instantaneous scale of diffusion $K_h(\ell) = \langle K_r | \ell_{\min} < \ell < \ell_{\max} \rangle$, where ℓ_{\min} and ℓ_{\max} define the limits for each scale bin (300-m-wide bins were used here).

III. RESULTS AND DISCUSSION

A. Effects of deep-water dispersant in the near field

Snapshots of instantaneous rising near-field plumes are shown in Figs. 1(b) and 1(c) for the cases without and with dispersant application at the wellhead, respectively. The average peel height from the simulation was 430 ± 26 m, which is on the same order of magnitude but about 20% smaller than the lower bound estimated for the DWH using an integral plume model (between 538 and 624 m [38]). Similarly, the average trap height from the simulations was 260 ± 16 m, being 15% smaller than the lower bound estimated from the same model (between 307 and 366 m [38]) and 16% smaller than the trap height estimated from measurements on May 30, 2010 [see Fig. 4(a) in Socolofsky *et al.* [38]]. We note that the shift in the density profile described in the methods section causes the peel and trap heights to decrease by about 20 and 10 m, respectively, and cannot be considered the main source of discrepancy. Fabregat *et al.* [20,46] showed that the precession effects caused by Coriolis tend to reduce the trap and peel heights, which may be the reason for the discrepancies between the LES results presented here and the integral plume model. We consider this agreement rather good given the uncertainties in the estimates from observations and the different strengths of the integral plume model and the present model (each being better in some aspects of the problem and worse in others).

Both plumes behaved similarly in the initial stage, when the oil plume raised together with the bubble plume as the buoyancy of the oil droplets was negligible compared to the flow driven by the gas bubbles. After the peeling process took place, the behavior of the two plumes was very different. For the simulation without dispersant at the wellhead [Fig. 1(b)], the oil plume continued to rise driven by its own buoyancy and reached the surface about 10 h after the release started. This surfacing time was in agreement with the 3 to 10-h window for the DWH spill [51]. Note that because the oil moved along with the gas in the initial stage (i.e., up to the peel height), the surfacing time was significantly smaller than an estimate based only on the oil rise velocity (which would yield 16.7 h in this case). Thus, the dynamics of peeling and intrusion layer formation played an important role in the surfacing time, and current estimates based on rise velocity alone (see, e.g., Ref. [51]) may have biased oil droplet size estimation towards larger diameters (in the present case, such an approach would yield an oil droplet size $d_o \approx 1.2$ mm, an overestimation of approximately 70%). In addition, the horizontal area of the plume once it reached the surface was also strongly influenced by these dynamics. As seen in Fig. 1(b), the large increase in the width of the oil plume during the peeling process defined the geometry of the rising oil plume and played a critical role in determining the lateral size of the oil plume that arrived in the OML. In the present case, the surfacing plume diameter was about 1 km, which is 37.5% smaller than the observed value of about 1.6 km [51]. This underprediction of the surfacing area was likely caused by the use of a single oil droplet size in the simulation (as opposed to a distribution of sizes).

The reduction in droplet size caused by the dispersant applied at the wellhead had important effects on the plume behavior after the peeling process. In this case, due to its low buoyancy, most of the oil was trapped in the intrusion layer (and even transported below the trap height by buoyancy-driven oscillations in the flow), as seen in Fig. 1(c) 18.9 h after the initial release. After the peeling, the rise of the oil plume was mostly driven by the very small rise velocity of the oil droplets (the exception being mostly due to oscillations caused by the transient initiation of the bubble plume dynamics). If the oil droplets were to rise from the trap height propelled by their own buoyancy, the surfacing time would be between 16 and 17 days in this case, providing ample time for biodegradation.

B. Effects of surface dispersant in the far field

As suggested by the small D_b number, as the oil reached the ocean surface it collected on shallow layers in regions of surface convergence [Fig. 1(a)]. Even though the droplets did not coalesce into an oil slick in the present simulation, the droplets had enough buoyancy that their behavior was approximately the same as that of a true slick on the surface, with almost all the oil being trapped on

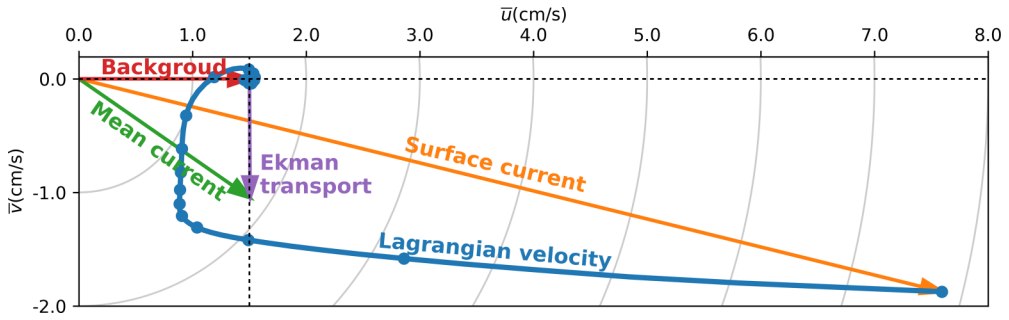


FIG. 2. Hodograph of mean Lagrangian velocity (Eulerian velocity of ocean current plus Stokes drift velocity) illustrating the Ekman spiral. The Lagrangian velocity converges to the background flow velocity (red vector) at the bottom of the far-field domain. The surface current (orange), the mean Ekman transport velocity in the OML (purple), and the mean current in the OML (green) are also indicated. The dot markers in the hodograph are 5 m apart with the first one being at $z = -0.5$ m.

the top layer of the model. As a consequence, oil concentrations on the surface were much higher than within the rising plume underneath (this difference was as large as 2 to 3 orders of magnitude). The plume of large droplets, as a true slick, was mostly transported by the surface current. In this sense, it is important to bear in mind that the mean velocity presented sharp gradients near the surface. The hodograph of the mean Lagrangian velocity (i.e., the fluid velocity plus the Stokes drift velocity) for the present simulation is shown in Fig. 2, illustrating the very large changes in mean horizontal flow speed and direction in the upper layers of the OML (with $\bar{u}_h \approx 7.8$ cm/s in the first grid point at $z = -0.5$ m, $\bar{u}_h \approx 3.2$ cm/s at $z = -5.5$ m, and $\bar{u}_h \leq 2$ cm/s below $z = -10.5$ m). For such shallow plumes, an accurate representation of the near-surface velocity gradients is critical.

Time evolutions of the oil patch initially within the target area are shown in Fig. 3 without and with application of dispersants. Because the application of dispersants mixed the oil into the water column, the vertically integrated plume (i.e., integrated between $z = -150$ m and the surface) was the appropriate quantity to characterize horizontal transport of oil. The differences between the two patches 18 h after the application of dispersant were striking. For the large oil droplets corresponding to the scenario without application of surface dispersant [Figs. 3(a)–3(c)], the plume continued traveling more or less in the direction of the surface current, and its lateral spread was quite small. Because almost all the oil was floating on the ocean surface, the vertically integrated plume showed the same fingered pattern seen in the surface plume [Fig. 1(a)]. A significant contribution to the deformation of the shape of the oil patch originated from the large eddies, which imposed a low-frequency straining and destraining cycle. The application of dispersant, here represented by a reduction in droplet size, significantly reduced the horizontal velocity of the oil patch and increased its lateral spread [Figs. 3(d)–3(f)]. In particular, the horizontal location of the center of mass of the patch was almost stationary during the second and third 6-h periods displayed in the figure. The final pattern for the entire plume after surface application of dispersant in the target area is also shown in Fig. 3(g), illustrating the modification of the oil transport due to dispersants: the oil patch that should have been at the surface in the gap around $x = 6.5$ km was nearly stationary and spreading laterally near $x = 3$ km.

A quantitative analysis of the time evolution of the oil patches is displayed in Fig. 4. For the case with no application of dispersant, the vertical position of the center of mass was at $z_{cm} \approx 0.5$ m at all times, confirming that the vast majority of the oil remained in the top vertical level of the model (note that the vertical grid spacing is $\Delta z = 1$ m for the far-field domain). In the case with dispersant, the center of mass started moving down immediately after the application, equilibrating around $z_{cm} \approx 18$ m after approximately 6 h (which corresponded to about 2.3 eddy turnover times estimated as z_i/u_*). The equilibration of the center of mass above the center of the OML confirmed

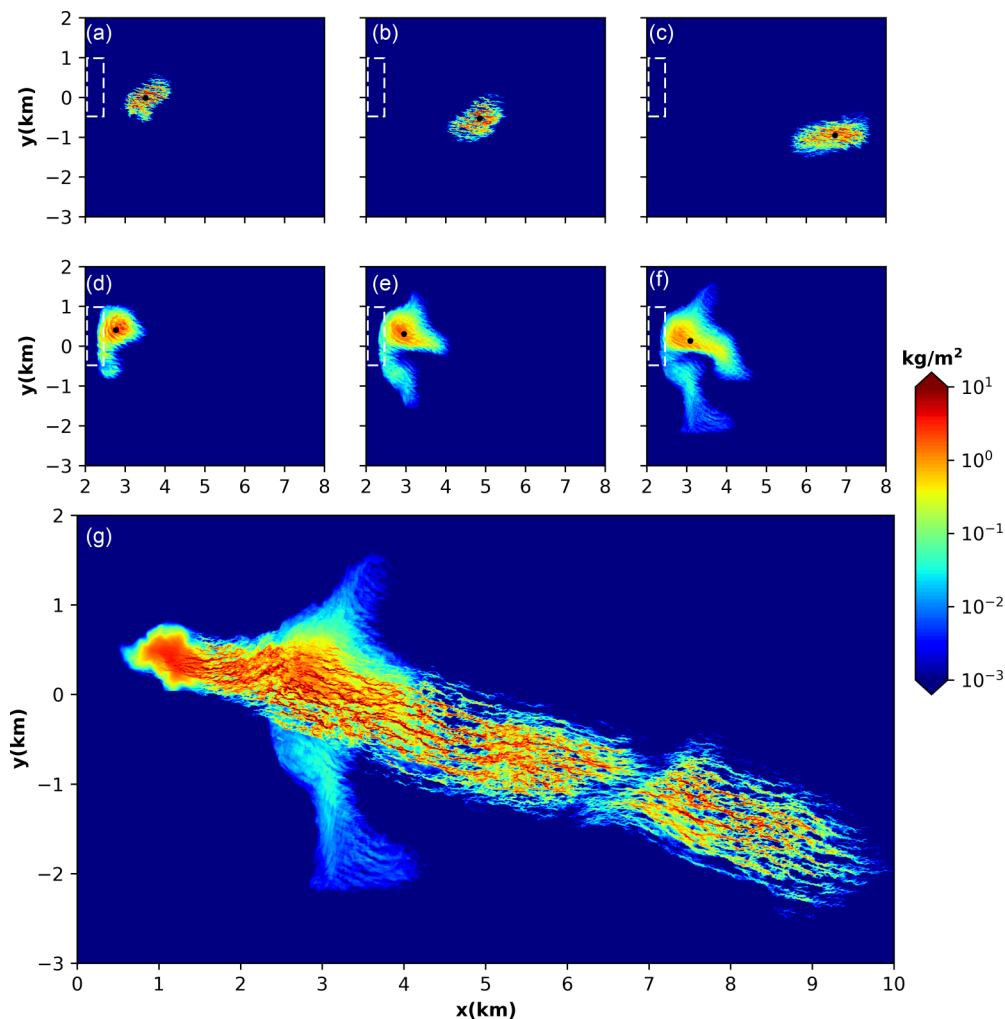


FIG. 3. Time evolution of vertically integrated oil concentration that was initially inside the rectangular patch marked by the dashed lines (a)–(f). The top row (a)–(c) is for the case without dispersant application, while the middle row (d)–(f) is with dispersant application. The three columns show results 6, 12, and 18 h after application of surface dispersant. The black dot in each panel represents the location of the center of mass of the oil patch. The bottom panel shows the total vertically integrated oil concentration for the entire plume 18 h after dispersant application in the target area.

the important role of droplet buoyancy in the vertical distribution of oil after surface dispersant application.

Figures 4(b) and 4(c) quantify the important changes in the mean horizontal transport of oil plumes caused by the application of dispersants. The plume without dispersant application moved approximately at the speed and the direction of the mean Lagrangian surface current (about 8 cm/s), with a low-frequency oscillation caused by the large eddies. The oil plume with dispersant application presented a much smaller advection velocity, causing the effects of the large eddies to appear as a very low-frequency oscillation. Nevertheless, the mean advection velocity approached the mean current speed (i.e., the vertically averaged Lagrangian velocity, including wind-driven component, Stokes drift, and the background flow) at the end of the simulation. So even though for a large portion of time (from 6 to 33 h) the speed of the plume with dispersant application was only about 1/8 of that without

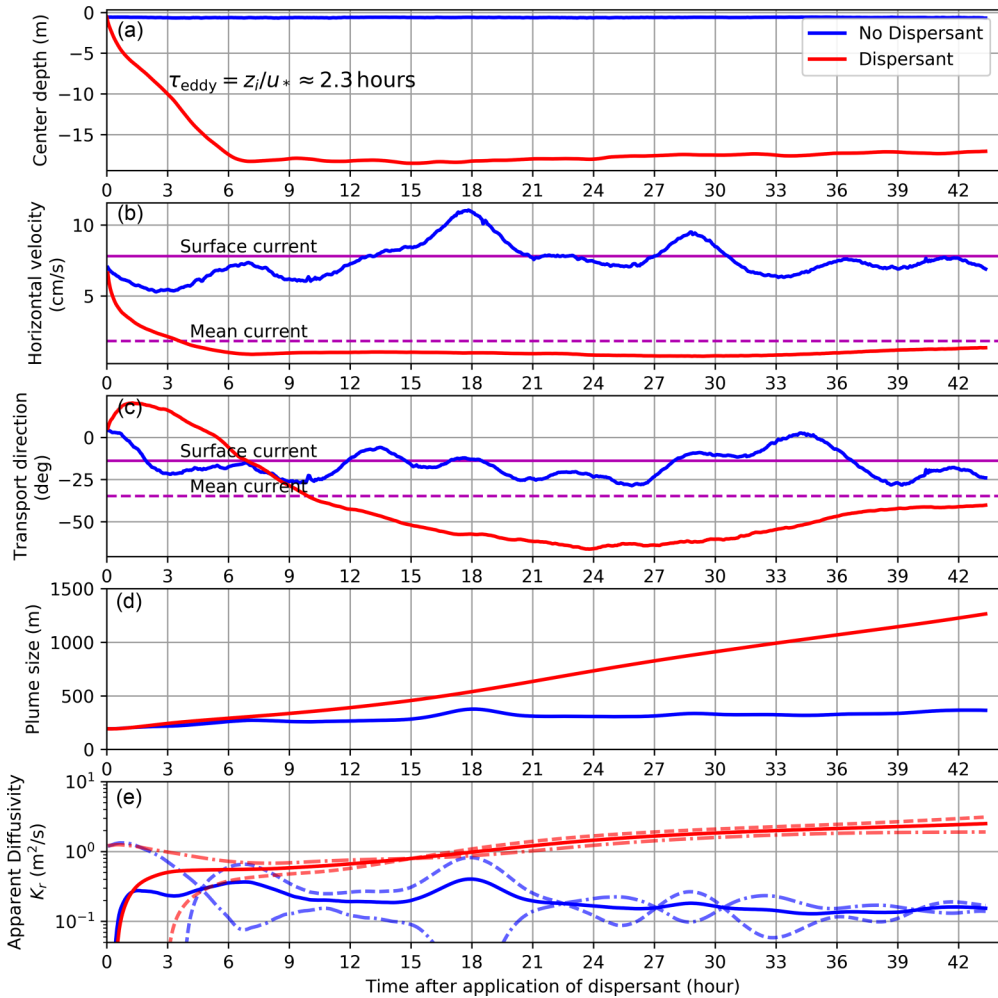


FIG. 4. Time evolution of statistics of oil patches with (red lines) and without (blue lines) application of surface dispersant: depth of the center of mass (a), horizontal advection speed of the center of mass (b), horizontal advection direction of center of mass (c), horizontal patch size (d), and the total apparent diffusivity (solid lines) and its components in x (dashed lines) and y (dashed-dotted lines) directions (e).

dispersant, it is reasonable to expect that over long periods the ratio will be closer to $1/4$ (the ratio of mean current speed over mean surface current speed). In addition to this much slower advection, the results also showed that the mean transport direction for the two oil plumes was different, with the original plume without dispersant moving in a direction approximately aligned with the surface current and the plume with dispersant approaching the direction of the mean current.

The time evolution of the horizontal patch size [Fig. 4(d)] showed that while the plume with dispersant grew to 6 times its original size in 43 h, the plume without application of dispersants grew to only about 1.5 times its original size. The growth of the latter was clearly inhibited by Langmuir turbulence, which acted to maintain very high oil concentrations within the localized convergence zones at the surface—a phenomenon referred to by Yang *et al.* [21] as “inhibition of oil plume dilution by Langmuir circulation.” In addition, the plume size did not always grow with time, showing some clear periods in which its size decreased as the patch was “squeezed” in straining regions between two large-scale eddies (this occurred in synchrony with the larger transport velocities associated with

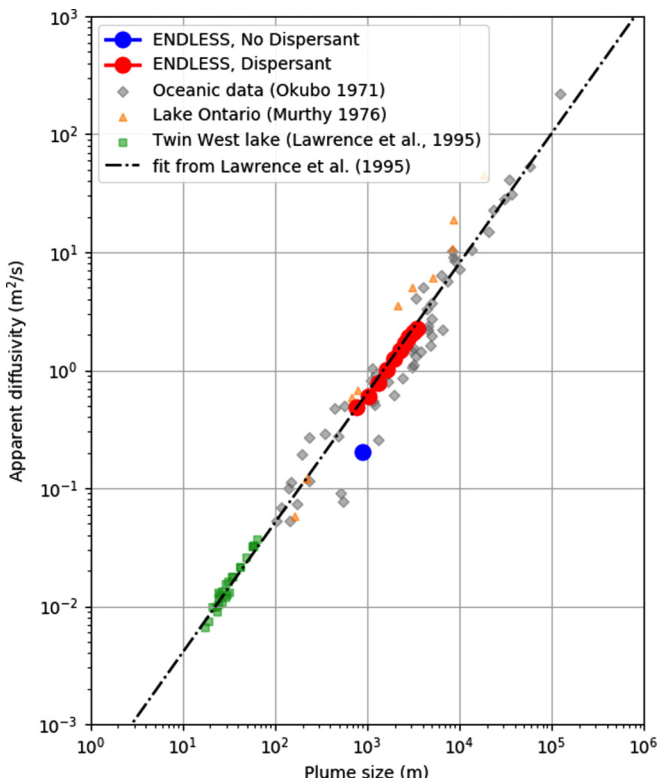


FIG. 5. Apparent diffusivity is shown against the scale of dispersion (defined here as $\ell = 3\sigma_r$) for the LES cases with and without dispersant (solid circles). In the same panel are also shown the fits of Lawrence *et al.* [28] using also data from Refs. [26,27].

the flow acceleration in these straining regions between large eddies). On the other hand, the plume affected by dispersant had its horizontal spread significantly increased by the directional shear within the Ekman spiral. These different behaviors were further quantified in terms of apparent diffusivities computed using Eq. (9) and Eq. (10) [Fig. 4(e)]. Note that in Fickian diffusion one would expect K_r to be constant and in Richardson diffusion $K_r \propto t^2$ [52]. While the total apparent diffusivity in the case with dispersant seems to follow somewhere in between these two cases, the surface slick without dispersant shows a small decrease of K_r with time.

The components of apparent diffusivity in x and y directions are also shown in Fig. 4(e). In general, for large times, there is not much directional dependence, and the lateral diffusivity is approximately isotropic. This is particularly clear for the plume with dispersant. For the plume without dispersant, the plume is very sensitive to the straining and destraining cycle imposed by the large eddies, which yields oscillations in apparent diffusivity out of phase by approximately 180° (this effect, at times, leads to one instance of negative diffusivity representing a very strong straining of the plume). Perhaps the most interesting feature is the crossing between the two diffusivities for the plume without dispersant, which suggest that the initial preferential growth in the y direction seen in Figs. 3(e)–3(f) is a transient effect. Indeed, the shape of the plume after 40 h is much more symmetric (not shown).

Instantaneous apparent diffusivities shown in Fig. 4(e) were averaged conditioned on the instantaneous plume scale yielding a scale-dependent $K_h(\ell)$. For the case without dispersant, the plume scale did not change much during the simulation period, and all points were averaged together, yielding one single value of K_h . For the case with dispersant, the plume scale increased significantly

yielding several points. These results are shown in Fig. 5 together with classic data from dye dispersion in shallow water illustrating the increase in diffusivity with increasing plume scale [26–28]. For the case without dispersant, the apparent diffusivity lies perfectly on top of the best fit from Lawrence *et al.* [28], suggesting the same scaling relation $K_h \approx 1.1 \times 10^{-3} \ell^{1.1}$ (with K_h in m^2/s and ℓ in m). This is expected, as the small droplets that result from the dispersant application have very small D_b number and behave similarly to a passive tracer (such as the dye used in the field observations). The excellent agreement between the numerical simulations using ENDLESS presented here and the observational data for plumes of size in the approximate range 500 to 5000 m also provides further support to the use of ENDLESS as a viable framework to study multiscale plumes. As expected from Fig. 4(e), the apparent diffusivity without dispersant is much smaller. Thus, application of dispersant increased the horizontal diffusivity by a factor of about 2.5 times for a similar plume size, and as much as 11 times if all 43 h are included.

IV. CONCLUSIONS

In this study, we performed high-resolution simulations of the oil transport from a deep-water blowout using the LES technique. This turbulence-resolving simulation is notable in including both the near-field multiphase plume rising through the water column and the far-field oil slick transport on the ocean surface. Idealized simulations designed based on the conditions reported for the DWH accident were employed to study the effects of dispersant application at the wellhead and at the ocean surface on fluid mechanical processes that govern oil transport. Results from the near-field domain were in reasonable agreement with observations from the DWH accident available in the literature, building some confidence in the modeling framework employed here.

The near-field portion of the simulation showed that plume dynamics plays an important role on the surfacing time of oil droplets, and that estimating droplet sizes from surfacing time based on droplet slip velocity alone can lead to large overprediction (about 70% for the specific case studied here). In addition, the wellhead application of dispersant simulated here was very effective in trapping most of the oil in the deep-water intrusion. It must be noted that this effectiveness is strongly dependent on the droplet size distribution prior to dispersant application, and that if the original oil plume is composed mostly of small droplets, dispersant application will obviously have weaker impact on the oil transport. Furthermore, environmental conditions can impact the effectiveness of the oil trapping promoted by the dispersant application. Two critical components that control the oil trapping in the present simulation are the dynamics of the buoyant plume and the presence of background. Given that even the weak background flow employed here was enough to effectively separate the oil droplets from the bubble plume, it is unlikely that ocean conditions will be so stagnant that the separation will not occur. The dynamics of the buoyant plume depends mostly on stratification, buoyancy flux (associated with oil and gas release rate at the wellhead), and bubble size. These parameters are combined in the nondimensional slip velocity U_N and control the characteristics of the peel zone and intrusion layer formation [45]. Numerical simulations suggest that, at least within the interval $0.53 < U_N < 3.53$ (and possibly beyond these limits), more than 80% of the fluid mass within the plume peels off into the intrusion [8], providing the first necessary step for the oil trapping. Thus, very large changes in stratification, oil and gas release, or bubble size would be needed to significantly impact the results obtained here. We also note that small variations in U_N would impact the characteristics of the intrusion, and thus the depth at which the oil droplets start ascending by their own rise velocity (surfacing time can be estimated from their rise velocity and the depth of the intrusion layer). Finally, the dynamics of the buoyant plume could be significantly altered by the Coriolis effect [20,46] or by the presence of strong background flow. While the Coriolis effect is known to become large at $R_o \leq 10$ [20], not much is known about the effect of strong background flow on the plume dynamics.

Results from the far-field domain showed that the desired vertical mixing of the surface oil slick within the OML promoted by chemical dispersants to enhance biodegradation also caused the oil plume to experience different physical processes, which lead to a significant reduction of

mean horizontal transport speeds and an increase in the horizontal spread of the oil. For the present case, with idealized large-scale flow, the mean horizontal transport speed was reduced by a factor of approximately 4, and the horizontal diffusivity was increased by a factor of 10 or more. The magnitudes of these changes depend on local ocean conditions and on the vertical distribution of oil in the water column. More specifically, the changes reported here rely on the fact that before dispersant application the oil will form slicks and stay mostly on the ocean surface, and after application it will be fairly well mixed within the OML. The formation of slicks is the typical behavior unless some external process (such strong wave breaking) can promote the breakup of the slick. The mixing of small droplets resulting from the dispersant application requires strong fluctuations in vertical velocity near the ocean surface, which in the present case the mixing is produced by the Langmuir cells and quantified in terms of the drift-to-buoyancy parameter [21]. The wave conditions adopted here are representative of relatively protected environments such as the Gulf of Mexico, with an approximate equilibrium between wind and wave, resulting in Langmuir number around 0.3 [47,48]. Under such conditions, $D_b > 10$ provides a reasonable criterion for relatively well-mixed droplet concentration profiles [21] and allows a rough estimate of maximum droplet sizes for well-mixed conditions given a fixed wave field. For less protected ocean regions, the presence of swell (i.e., waves generated remotely and independent of the local wind) has to be considered. The potential misalignment between swell and local winds can lead to a strong reduction of the vertical mixing [24], and one would probably have to define an equivalent D_b number for these conditions.

Accurate prediction of these changes via numerical modeling requires high-resolution simulations capable of representing the sharp gradients in oil concentration and mean horizontal velocity magnitude and direction in the uppermost 10 or 20 m of the OML. It is possible that adequate parametrizations can be developed to incorporate these effects in regional models (e.g., via modified KPP parametrizations [22]). Nevertheless, for models based on simple parametrization of the vertical distribution of oil [53], as a general rule of thumb it seems reasonable to estimate that the oil slick on the surface moves with the surface Lagrangian velocity, and after application of dispersant it will move with the vertically averaged Lagrangian velocity in the OML (assuming that droplets are small enough to be uniformly distributed within the OML). Both velocities can be estimated from regional models yielding, at least, a first estimate of the effects of surface dispersant application on oil transport. As for the enhanced lateral diffusivity, it may be possible to extend the theory of shear dispersion to a case in which there is also directional shear.

Data are publicly available through the Gulf of Mexico Research Initiative Information and Data Cooperative (GRIIDC) [54].

ACKNOWLEDGMENT

This research was made possible by a grant from the Gulf of Mexico Research Initiative.

-
- [1] P. Eckle, P. Burgherr, and E. Michaux, Risk of large oil spills: A statistical analysis in the aftermath of Deepwater Horizon, *Environ. Sci. Technol.* **46**, 13002 (2012).
 - [2] E. B. Kujawinski, M. C. K. Soule, D. L. Valentine, A. K. Boysen, K. Longnecker, and M. C. Redmond, Fate of dispersants associated with the Deepwater Horizon oil spill, *Environ. Sci. Technol.* **45**, 1298 (2011).
 - [3] National Research Council, *Oil Spill Dispersants: Efficacy and Effects* (National Academies Press, Washington, DC, 2005).
 - [4] R. S. Judson, M. T. Martin, D. M. Reif, K. A. Houck, T. B. Knudsen, D. M. Rotroff, M. Xia, S. Sakamuru, R. Huang, P. Shinn, C. P. Austin, R. J. Kavlock, and D. J. Dix, Analysis of eight oil spill dispersants

- using rapid, in vitro tests for endocrine and other biological activity, *Environ. Sci. Technol.* **44**, 5979 (2010).
- [5] M. J. Hemmer, M. G. Barron, and R. M. Greene, Comparative toxicity of eight oil dispersants, Louisiana sweet crude oil (LSC), and chemically dispersed LSC to two aquatic test species, *Environ. Toxicol. Chem.* **30**, 2244 (2011).
- [6] R. Rico-Martínez, T. W. Snell, and T. L. Shearer, Synergistic toxicity of Macondo crude oil and dispersant Corexit 9500A® to the *Brachionus plicatilis* species complex (Rotifera), *Environ. Pollut.* **173**, 5 (2013).
- [7] S. A. Socolofsky, T. Bhaumik, and D.-G. Seol, Double-plume integral models for near-field mixing in multiphase plumes, *J. Hydraul. Eng.* **134**, 772 (2008).
- [8] D. Yang, B. Chen, S. A. Socolofsky, M. Chamecki, and C. Meneveau, Large-eddy simulation and parameterization of buoyant plume dynamics in stratified flow, *J. Fluid Mech.* **794**, 798 (2016).
- [9] T. Asaeda and J. Imberger, Structure of bubble plumes in linearly stratified environments, *J. Fluid Mech.* **249**, 35 (1993).
- [10] S. A. Socolofsky and E. E. Adams, Liquid volume fluxes in stratified multiphase plumes, *J. Hydraul. Eng.* **129**, 905 (2003).
- [11] R. R. Lessard and G. DeMarco, The significance of oil spill dispersants, *Spill Sci. Technol. Bull.* **6**, 59 (2000).
- [12] M. Maltrud, S. Peacock, and M. Visbeck, On the possible long-term fate of oil released in the Deepwater Horizon incident, estimated using ensembles of dye release simulations, *Environ. Res. Lett.* **5**, 035301 (2010).
- [13] H. S. Huntley, B. L. Lipphardt Jr., and A. D. Kirwan Jr., Surface drift predictions of the *Deepwater Horizon* spill: The Lagrangian perspective, in *Monitoring and Modeling the Deepwater Horizon Oil Spill: A Record-Breaking Enterprise*, edited by Y. Liu, A. Macfadyen, Z.-G. Ji, and R. H. Weisberg (Wiley, New York, 2013), Vol. 195, p. 179.
- [14] M. Le Hénaff, V. H. Kourafalou, C. B. Paris, J. Helgers, Z. M. Aman, P. J. Hogan, and A. Srinivasan, Surface evolution of the Deepwater Horizon oil spill patch: Combined effects of circulation and wind-induced drift, *Environ. Sci. Technol.* **46**, 7267 (2012).
- [15] C. B. Paris, M. Le Hénaff, Z. M. Aman, A. Subramaniam, J. Helgers, D.-P. Wang, V. H. Kourafalou, and A. Srinivasan, Evolution of the Macondo well blowout: Simulating the effects of the circulation and synthetic dispersants on the subsea oil transport, *Environ. Sci. Technol.* **46**, 13293 (2012).
- [16] M. C. Boufadel, A. Abdollahi-Nasab, X. Geng, J. Galt, and J. Torlapati, Simulation of the landfall of the Deepwater Horizon oil on the shorelines of the Gulf of Mexico, *Environ. Sci. Technol.* **48**, 9496 (2014).
- [17] J. M. Testa, E. E. Adams, E. W. North, and R. He, Modeling the influence of deep water application of dispersants on the surface expression of oil: A sensitivity study, *J. Geophys. Res. Oceans* **121**, 5995 (2016).
- [18] A. Fabregat, W. K. Dewar, T. M. Özgökmen, A. C. Poje, and N. Wienders, Numerical simulations of turbulent thermal, bubble and hybrid plumes, *Ocean Model.* **90**, 16 (2015).
- [19] B. Fraga, T. Stoesser, C. C. K. Lai, and S. A. Socolofsky, A LES-based Eulerian–Lagrangian approach to predict the dynamics of bubble plumes, *Ocean Model.* **97**, 27 (2016).
- [20] A. Fabregat, A. C. Poje, T. M. Özgökmen, and W. K. Dewar, Effects of rotation on turbulent buoyant plumes in stratified environments, *J. Geophys. Res. Oceans* **121**, 5397 (2016).
- [21] D. Yang, M. Chamecki, and C. Meneveau, Inhibition of oil plume dilution in Langmuir ocean circulation, *Geophys. Res. Lett.* **41**, 1632 (2014).
- [22] D. Yang, B. Chen, M. Chamecki, and C. Meneveau, Oil plumes and dispersion in Langmuir, upper-ocean turbulence: Large-eddy simulations and K-profile parameterization, *J. Geophys. Res. Oceans* **120**, 4729 (2015).
- [23] B. Chen, D. Yang, C. Meneveau, and M. Chamecki, Effects of swell on transport and dispersion of oil plumes within the ocean mixed layer, *J. Geophys. Res. Oceans* **121**, 3564 (2016).
- [24] B. Chen, D. Yang, C. Meneveau, and M. Chamecki, ENDLESS: An extended nonperiodic domain large-eddy simulation approach for scalar plumes, *Ocean Model.* **101**, 121 (2016).
- [25] H. Stommel, Horizontal diffusion due to oceanic turbulence, *J. Mar. Res.* **8**, 199 (1949).
- [26] A. Okubo, Oceanic diffusion diagrams, *Deep Sea Research and Oceanographic Abstracts* **18**, 789 (1971).

- [27] C. R. Murthy, Horizontal diffusion characteristics in Lake Ontario, *J. Phys. Oceanogr.* **6**, 76 (1976).
- [28] G. A. Lawrence, K. I. Ashley, N. Yonemitsu, and J. R. Ellis, Natural dispersion in a small lake, *Limnol. Oceanogr.* **40**, 1519 (1995).
- [29] A. D. D. Craik and S. Leibovich, A rational model for Langmuir circulations, *J. Fluid Mech.* **73**, 401 (1976).
- [30] A. D. D. Craik, The generation of Langmuir circulations by an instability mechanism, *J. Fluid Mech.* **81**, 209 (1977).
- [31] S. Leibovich, On the evolution of the system of wind drift currents and Langmuir circulations in the ocean. Part 1. Theory and averaged current, *J. Fluid Mech.* **79**, 715 (1977).
- [32] J. C. McWilliams, P. P. Sullivan, and C.-H. Moeng, Langmuir turbulence in the ocean, *J. Fluid Mech.* **334**, 1 (1997).
- [33] J. Ferry and S. Balachandar, A fast Eulerian method for disperse two-phase flow, *Int. J. Multiphase Flow* **27**, 1199 (2001).
- [34] J. Smagorinsky, General circulation experiments with the primitive equations: I. The basic experiment, *Mon. Weather Rev.* **91**, 99 (1963).
- [35] D. K. Lilly, The representation of small scale turbulence in numerical simulation experiments, in *IBM Scientific Computing Symposium on Environmental Sciences* (Yorktown Heights, 1967), pp. 195–210.
- [36] E. Bou-Zeid, C. Meneveau, and M. Parlange, A scale-dependent lagrangian dynamic model for large eddy simulation of complex turbulent flows, *Phys. Fluids (1994–present)* **17**, 025105 (2005).
- [37] D.-G. Seol, D. B. Bryant, and S. A. Socolofsky, Measurement of behavioral properties of entrained ambient water in a stratified bubble plume, *J. Hydraul. Eng.* **135**, 983 (2009).
- [38] S. A. Socolofsky, E. E. Adams, and C. R. Sherwood, Formation dynamics of subsurface hydrocarbon intrusions following the Deepwater Horizon blowout, *Geophys. Res. Lett.* **38**, 2 (2011).
- [39] R. Clift, J. R. Grace, and M. E. Weber, *Bubbles, Drops, and Particles* (Courier Corporation, Indianapolis, 2005).
- [40] L. Zheng and P. D. Yapa, Buoyant velocity of spherical and nonspherical bubbles/droplets, *J. Hydraul. Eng.* **126**, 852 (2000).
- [41] B. Lehr, S. Nristol, and A. Possolo, Oil budget calculator—Deepwater Horizon, technical documentation: A report to the National Incident Command, Federal Interagency Solutions Group (2010), https://www.restorethegulf.gov/sites/default/files/documents/pdf/OilBudgetCalc_Full_HQ-Print_111110.pdf.
- [42] E. E. Adams, S. A. Socolofsky, and M. Boufadel, Comment on “Evolution of the Macondo well blowout: Simulating the effects of the circulation and synthetic dispersants on the subsea oil transport,” *Environ. Sci. Technol.* **47**, 11905 (2013).
- [43] Z. M. Aman and C. B. Paris, Response to comment on “Evolution of the Macondo well blowout: Simulating the effects of the circulation and synthetic dispersants on the subsea oil transport,” *Environ. Sci. Technol.* **47**, 11906 (2013).
- [44] J. Beyer, H. C. Trannum, T. Bakke, P. V. Hodson, and T. K. Collier, Environmental effects of the Deepwater Horizon oil spill: A review, *Mar. Pollut. Bull.* **110**, 28 (2016).
- [45] S. A. Socolofsky and E. E. Adams, Role of slip velocity in the behavior of stratified multiphase plumes, *J. Hydraul. Eng.* **131**, 273 (2005).
- [46] A. F. Tomàs, A. C. Poje, T. M. Özgökmen, and W. K. Dewar, Numerical simulations of rotating bubble plumes in stratified environments, *J. Geophys. Res. Oceans* **122**, 6795 (2017).
- [47] M. Li, C. Garrett, and E. Skillingstad, A regime diagram for classifying turbulent large eddies in the upper ocean, *Deep Sea Res. I: Oceanogr. Res. Papers* **52**, 259 (2005).
- [48] P. P. Sullivan and J. C. McWilliams, Dynamics of winds and currents coupled to surface waves, *Annu. Rev. Fluid Mech.* **42**, 19 (2010).
- [49] L. Zhao, M. C. Boufadel, T. King, B. Robinson, F. Gao, S. A. Socolofsky, and K. Lee, Droplet and bubble formation of combined oil and gas releases in subsea blowouts, *Marine Pollution Bull.* **120**, 203 (2017).
- [50] L. F. Richardson, Atmospheric diffusion shown on a distance-neighbour graph, *Proc. R. Soc. London A* **110**, 709 (1926).
- [51] T. B. Ryerson, R. Camilli, J. D. Kessler, E. B. Kujawinski, C. M. Reddy, D. L. Valentine, E. Atlas, D. R. Blake, J. De Gouw, S. Meinardi, D. D. Parrish, J. Peischl, J. S. Seewald, and C. Warneke, Chemical data

- quantify Deepwater Horizon hydrocarbon flow rate and environmental distribution, *Proc. Natl. Acad. Sci. USA* **109**, 20246 (2012).
- [52] E. Gray and T. E. Pochapsky, Surface dispersion experiments and Richardson's diffusion equation, *J. Geophys. Res.* **69**, 5155 (1964).
- [53] M. Zeinstra-Helfrich, W. Koops, and A. J. Murk, Predicting the consequence of natural and chemical dispersion for oil slick size over time, *J. Geophys. Res. Oceans* **122**, 7312 (2017).
- [54] C. Menevean and M. Chamecki, Data for "Effects of dispersant on oil transport within the ocean mixed layer," <https://doi.org/10.7266/N70000F7> (2018).

Correction: The data availability statement has now been relocated and anchored with complete source information.